Hindawi
Shock and Vibration
Volume 2020, Article ID 8843524, 17 pages
https://doi.org/10.1155/2020/8843524

Research Article

Study on Simplified Model and Numerical Solution of High-Speed Angular Contact Ball Bearing

Guang Zeng,[1] Chunjiang Zhao ,[1] Xiaokai Yu,[2] Biao Sun,[1] Zhigang Xiao,[1] Qiang Bian,[1] and Bingyang Liu[1]

[1]*School of Mechanical Engineering and Engineering Research Center of Heavy Machinery Ministry of Education, Taiyuan University of Science and Technology, Taiyuan 030024, China*
[2]*Department of Product Development, Luoyang Bearing Science and Technology Co., Ltd.,, Luoyang 471000, China*

Correspondence should be addressed to Chunjiang Zhao; zhaochj75@163.com

Received 1 July 2020; Revised 8 October 2020; Accepted 11 November 2020; Published 8 December 2020

Academic Editor: Anindya Ghoshal

Copyright © 2020 Guang Zeng et al. This is an open access article distributed under the Creative Commons Attribution License, which permits unrestricted use, distribution, and reproduction in any medium, provided the original work is properly cited.

For the calculation model of high-speed angular contact bearing has many variables, the large root difference exists, and the Newton iterative method solving the convergence depends on the initial value problems; thus, the simplified calculation model is proposed and the algorithm is improved. Firstly, based on the nonlinear equations of variables recurrence method of the high-speed angular contact ball bearing calculation model, it is proved that the ultimate fundamental variables of calculation model are the actual inner and outer contact angles, the axial and radial deformations. According to this reason, the nonlinear equations are deformed and deduced, and the number of equations is reduced from $4Z + 2$ to $2Z + 2$ (Z represents the number of rolling bodies); a simplified calculation model is formed. Secondly, according to the small dependence of the artificial bee colony algorithm on the initial value, an improved artificial bee colony algorithm is proposed for the large root difference characteristics of high-speed ball bearings. The validity of the improved algorithm is verified by standard test function. The algorithm is used to solve the high-speed angular contact ball bearing calculation model. Finally, the deformations of high-speed angular contact ball bearings are compared and verified by experiments, and the results of improved algorithm show good agreement with the experiments results.

1. Introduction

Although the angular contact ball bearing has a simple structure, the internal force and motion relationship become complicated due to the gyroscopic moment and centrifugal force at high speed [1]. In order to study the dynamic characteristics of the ball bearing, Jones [2] first established a quasistatic model based on the raceway control theory and Hertz contact theory. Subsequently, Harris et al. [3] further improved the model, which is referred to as the Jones-Harris (J-H) model. Because the J-H model is effective and accurate for the calculation of internal load distribution, contact angle variation, fatigue life, and stiffness [4–11] of high-speed ball bearings, the model is still widely applied.

The J-H model consists of a series of deformed geometric equations, rolling element equilibrium equations, and inner ring equilibrium equations, which form a high-dimensional nonlinear equation [12]. The system consists of a total of $4Z + 2$ nonlinear equations [1]. In order to make J-H model solution more convenient, many scholars have conducted in-depth research. Antoine [13] proposed a new method for calculating contact angle of high-speed ball bearings under axial load. Zhang et al. [14] solved the dynamic characteristics of high-speed angular contact bearing based on various contact angles and hybrid theory. Kurvinen et al. [15] studied the method of solving the dynamic characteristics of angular contact bearings without considering gyroscopic moment and centrifugal force. Yu et al. [16] studied the particle swarm optimization (PSO) algorithm for solving the nonlinear equations of angular contact bearing. Wang et al. [17] studied the modeling and dynamic characteristics of angular contact bearings under axial, radial, and moment loads simultaneously.

Although these methods effectively improve the convergence of the original J-H method, they do not fundamentally reduce the computational complexity of the model. Fang et al. [18] simplified the calculation model by deriving the internal balance equation of the bearing, but the solution still uses the Newton-Raphson method. Although these algorithms have proved to be effective in solving nonlinear systems of equations [1, 19], there are still some shortcomings such as high dependence on initial values, slow convergence speed, and being easy to fall into premature convergence and early convergence when solving nonlinear equations with large root differences [20]. Nowadays, advanced algorithms such as Shuffled Frog Leading algorithm [21], firefly algorithm [22], and artificial bee colony algorithm [23] have emerged with the rapid development of computer algorithm technology. These algorithms can transform the problem of solving nonlinear equations into optimization problems. Therefore, if they can reduce the equations number, meanwhile adopting the improved swarm intelligence algorithm for high-speed angular contact bearing model, they can effectively reduce the computational complexity and convergence and realize the fast and accurate solution of the high-speed ball bearing model.

In order to solve the problem of too many nonlinear equations of high-speed angular contact bearing, the author determined the recursive relation among all variables in the model and deduced the calculation model according to the actual contact angle, axial deformation, and radical deformation. The number of solving equations is reduced from $4Z + 2$ to $2Z + 2$, which reduces the computational complexity by nearly half compared with the traditional algorithm. In addition, for the characteristics of large root difference of the angular contact ball bearing calculation, the artificial bee colony algorithm which initializes the food source in stages is adopted to improve the convergence precision and the solution speed of the solution. Finally, the deformation of angular contact ball bearings at high speed is compared and verified by experiments, and the improved algorithm results show good agreement with experiments results.

2. Establishing a Simplified Calculation Model

2.1. Traditional Computing Model. Solving the high-speed characteristics of angular contact ball bearings has to start from the contact deformation. Establishing the bearing deformation geometry equation, the rolling element balance equation, and the inner ring balance equation and then establishing the auxiliary equations including centrifugal force, gyroscopic moment, and contact angle are needed. Figure 1 is a schematic diagram of the rolling elements in the different ball angular position ψ_j; Figure 2 is a schematic diagram of rolling body force; Figure 3 shows the relative position relationships between the centers of the inner and outer raceways groove curvature and the rolling elements centers before and after the bearing is loaded (according to the inner ring rotation and the outer ring fixation). According to the literature [12], combined with Hertz contact theory, bearing motion, and force relationship and raceway control theory, the calculation model of high-speed angular contact ball bearing is given.

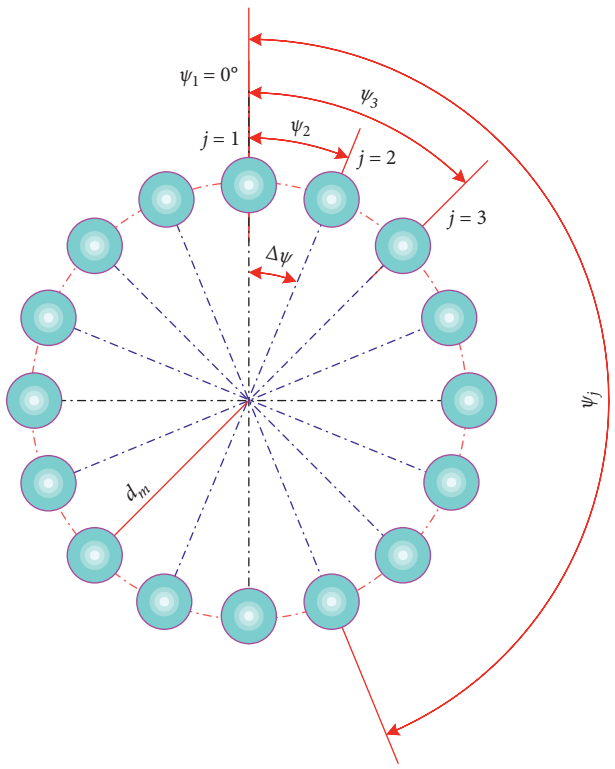

Figure 1: Position map of rolling elements at different azimuth angles ψ_j.

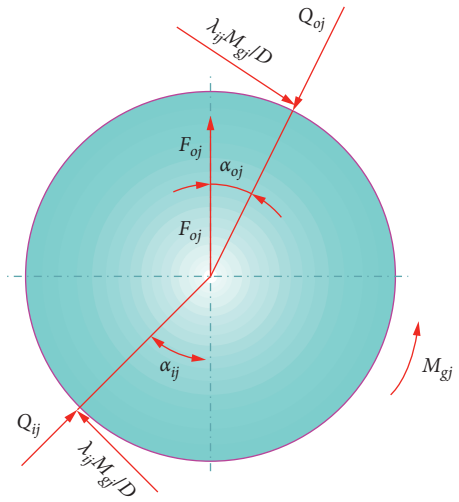

Figure 2: Schematic diagram of the rolling element.

2.1.1. Deformation Geometry Equation. Figure 3 shows that the axial distance A_{1j} and radial distance A_{2j} between the curvature centers of inner and outer raceway grooves in the ball angular position ψ_j are as follows:

$$A_{1j} = B\,D \sin\,\alpha^0 + \delta_\alpha + \Re_i\theta\cos\psi_j, \tag{1}$$

$$A_{2j} = B\,D\cos\,\alpha^0 + \delta_r\cos\psi_j, \tag{2}$$

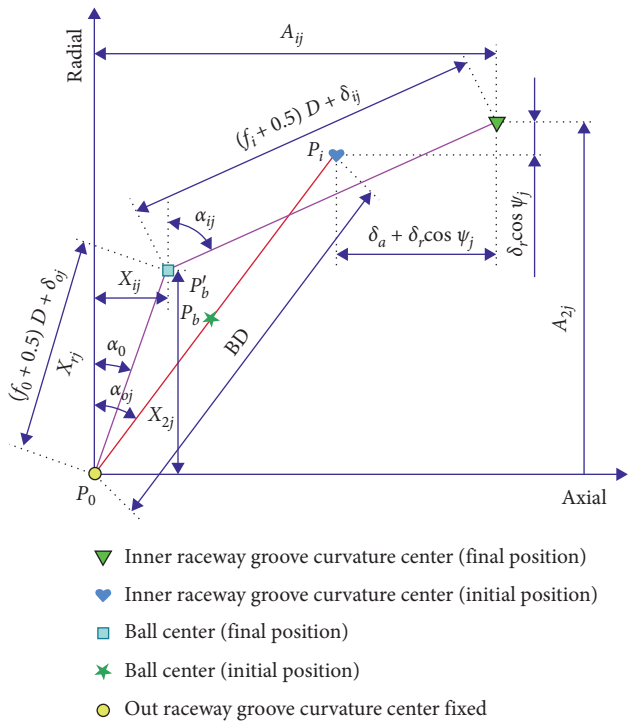

FIGURE 3: Schematic diagram of the change of the center position of the groove before and after the load.

where δ_a, δ_r, and θ, respectively, denote the relative axial deformation, relative radial deformation, and relative angular displacement of the inner and outer rings; $\mathfrak{R}_i$ denotes the radius of the groove curvature center trajectory of inner raceway; α^0 is the initial contact angle of the bearing.

The following geometric relationship can be determined from Figure 3:

$$\cos\alpha_{oj} = \frac{X_{2j}}{(f_o - 0.5)D + \delta_{oj}}, \tag{3}$$

$$\sin\alpha_{oj} = \frac{X_{1j}}{(f_o - 0.5)D + \delta_{oj}}, \tag{4}$$

$$\cos\alpha_{ij} = \frac{A_{2j} - X_{2j}}{(f_i - 0.5)D + \delta_{ij}}, \tag{5}$$

$$\sin\alpha_{ij} = \frac{A_{1j} - X_{1j}}{(f_i - 0.5)D + \delta_{ij}}. \tag{6}$$

In these equations, α is the contact angle of the bearing; f is the groove curvature of the bearing; the subscripts o and i are the outer ring and inner ring of the bearing, respectively; D is the ball diameter. According to the deformation geometric relationship between the components in Figure 3, combined with the Pythagorean theorem and (1) and (2), the position change relationship equation among the center of curvature of the rolling elements and the inner and outer grooves in the ball angular position ψ_j can be obtained:

$$\left(A_{1j} - X_{1j}\right)^2 + \left(A_{2j} - X_{2j}\right)^2 - \left[(f_i - 0.5)D + \delta_{ij}\right]^2 = 0, \tag{7}$$

$$X_{1j}^2 + X_{2j}^2 - \left[(f_o - 0.5)D + \delta_{oj}\right]^2 = 0. \tag{8}$$

2.1.2. Rolling Element Balance Equation. According to Hertz contact theory, the normal contact forces Q of the rolling body and the inner and outer rings at the contact points are as follows:

$$Q_{ij} = K_{ij}\delta_{ij}^{1.5}, \tag{9}$$

$$Q_{oj} = K_{oj}\delta_{oj}^{1.5}. \tag{10}$$

As shown in Figure 2, in the ball angular position ψ_j, the forced balance equations of rolling elements in the radial and axial can be written as

$$Q_{ij}\sin\alpha_{ij} - Q_{oj}\sin\alpha_{oj} - \frac{M_{gj}}{D}\left(\lambda_{ij}\cos\alpha_{ij} - \lambda_{oj}\cos\alpha_{oj}\right) = 0, \tag{11}$$

$$Q_{ij}\cos\alpha_{ij} - Q_{oj}\cos\alpha_{oj} + \frac{M_{gj}}{D}\left(\lambda_{ij}\sin\alpha_{ij} - \lambda_{oj}\sin\alpha_{oj}\right) + F_{oj} = 0, \tag{12}$$

where M_g is the gyro moment of the ball. Substituting (3)–(6), (9), and (10) into (11) and (12) yields

$$\frac{K_{ij}\delta_{ij}^{1.5}\left(A_{1j} - X_{1j}\right) - \left(\lambda_{ij}M_{gj}/D\right)\left(A_{2j} - X_{2j}\right)}{(f_i - 0.5)D + \delta_{ij}} + \frac{\left(\lambda_{oj}M_{gj}X_{2j}/D\right) - K_{oj}\delta_{oj}^{1.5}X_{1j}}{(f_o - 0.5)D + \delta_{oj}} = 0, \tag{13}$$

$$\frac{K_{ij}\delta_{ij}^{1.5}\left(A_{2j} - X_{2j}\right) - \left(\lambda_{ij}M_{gj}/D\right)\left(A_{1j} - X_{1j}\right)}{(f_i - 0.5)D + \delta_{ij}} - \frac{\left(\lambda_{oj}M_{gj}X_{1j}/D\right) + K_{oj}\delta_{oj}^{1.5}X_{2j}}{(f_o - 0.5)D + \delta_{oj}} + F_{cj} = 0. \tag{14}$$

2.1.3. Inner Ring Balance Equation. According to the force balance relationship and the moment load balance relationship of the bearing inner ring in the axial and radial directions, the inner ring balance equation can be obtained:

$$F_a - \sum_{j=1}^{j=z}\left(Q_{ij}\sin\alpha_{ij} - \frac{M_{gj}}{D}\lambda_{ij}\cos\alpha_{ij}\right) = 0,$$

$$F_r - \sum_{j=1}^{j=z}\left(Q_{ij}\cos\alpha_{ij} + \frac{M_{gj}}{D}\lambda_{ij}\sin\alpha_{ij}\right)\cos\psi_j = 0,$$

$$M - \sum_{j=1}^{j=z}\left[\left(Q_{ij}\sin\alpha_{ij} - \frac{M_{gj}}{D}\lambda_{ij}\cos\alpha_{ij}\right)\mathfrak{R}_i + f_i\lambda_{ij}M_{gj}\right]\cos\psi_j = 0. \tag{15}$$

Substituting (3)–(6), (9), and (10) into (16)–(18) results in

$$F_a - \sum_{j=1}^{j=z}\left[\frac{K_{ij}\delta_{ij}^{1.5}\left(A_{1j} - X_{1j}\right) - \left(\lambda_{ij}M_{gj}/D\right)\left(A_{2j} - X_{2j}\right)}{\left(f_i - 0.5\right)D + \delta_{ij}}\right] = 0, \tag{16}$$

$$F_r - \sum_{j=1}^{j=z}\left[\frac{K_{ij}\delta_{ij}^{1.5}\left(A_{2j} - X_{2j}\right) + \left(\lambda_{ij}M_{gj}/D\right)\left(A_{1j} - X_{1j}\right)}{\left(f_i - 0.5\right)D + \delta_{ij}}\right]\cos\psi_j = 0, \tag{17}$$

$$M - \sum_{j=1}^{j=z}\left[\frac{K_{ij}\delta_{ij}^{1.5}\left(A_{1j} - X_{1j}\right) - \left(\lambda_{ij}M_{gj}/D\right)\left(A_{2j} - X_{2j}\right)}{\left(f_i - 0.5\right)D + \delta_{ij}}\mathfrak{R}_i + f_i\lambda_{ij}M_{gj}\right]\cos\psi_j = 0, \tag{18}$$

where F_a, F_r, and M, respectively, are the axial, radial, and moment forces acting on the bearing. Given the initial iteration values of δ_a, δ_r, and θ, the iteration algorithm can be used to solve the nonlinear equations composed of formulas (7), (8), (13), and (14) in the ball angular position ψ_j and obtain X_{1j}, X_{2j}, δ_{ij}, and δ_{oj}. By substituting these into the nonlinear equations (16)–(18) in every ball angular position ψ_j, the values of the main unknowns δ_a, δ_r, and θ can be obtained. Then, the iteration of X_{1j}, X_{2j}, δ_{ij}, and δ_{oj} continued until the values of the main unknowns δ_a, δ_r, and θ meet the accuracy.

2.2. High-Speed Angular Contact Ball Bearings Calculation Model Analysis. Equations (7), (8), (13), (14), and (16)–(18) constitute a system of nonlinear equations, where there are $4Z+2$ equations. The calculation of contact stiffnesses K_{ij} and K_{oj}, centrifugal force F_{cj}, and gyroscopic moment M_{gj} of rolling elements and inner and outer rings at contact points all depends on the calculated values. And K_{ij}, K_{oj}, F_{cj}, and M_{gj} are functions of the actual internal and external contact angles α_{ij} and α_{oj}; the actual internal angle $\alpha_{ij}$and external contact angle α_{oj} are functions of X_{1j} and X_{2j}. Therefore, the variables in the dynamic characteristic equations are highly coupled, which makes the iterative calculation process very complicated and the calculation amount is extremely large. The initial value is not chosen properly, and it is difficult to converge or even not converge.

2.2.1. Variable Recursion Relation Analysis of Computational Model

(1) Variable Recursion Relation Analysis of Centrifugal Force F_{cj}. In ball angular position ψ_j, the centrifugal forces F_{cj} of the high-speed angular contact ball bearing rolling element can be expressed as follows:

$$F_{cj} = 2.26\times10^{-11}D^3d_mn_{mj}^2. \tag{19}$$

In the above formula, the formula for calculating the revolution speed $n_{mj}$of the rolling element is as follows:

$$n_{mj} = \frac{n_{ij}\left(1-\gamma_{ij}\right)\left(1+\gamma_{oj}\right)\left(\Omega_i \pm \Omega_o\right)}{\left(1+\gamma_{oj}\right)\cos\left(\alpha_{oj}-\beta_{oj}\right)+\left(1-\gamma_{oj}\right)\cos\left(\alpha_{oj}-\beta_{oj}\right)}. \tag{20}$$

According to the outer raceway control theory, the attitude angle $\beta_{oj}$of the rolling element is as follows:

$$\beta_{oj} = \arctan\left(\frac{\cos\alpha_{oj}\sin\alpha_{oj}}{\cos^2\alpha_{oj}+\gamma_{oj}}\right). \tag{21}$$

In the above formula, the formula for calculating the revolution speed γ_{oj} of the rolling element is as follows:

$$\gamma_{o(i)j} = \frac{D_w\cos\alpha_{o(i)j}}{d_m}. \tag{22}$$

As shown in Figure 4, based on the above analysis, the following variable transfer relationship can be obtained, "where the left side of the arrow is the function to the right of the arrow."

(2) Variable Recursion Relation Analysis of Gyroscopic Moment M_{gj}. In ball angular position ψ_j, the gyroscopic moment M_{gj} of the high-speed angular contact ball bearing can be expressed as

$$M_{gj} = 4.5\times10^{-11}D^5n_{bj}n_{mj}\sin\beta_j, \tag{23}$$

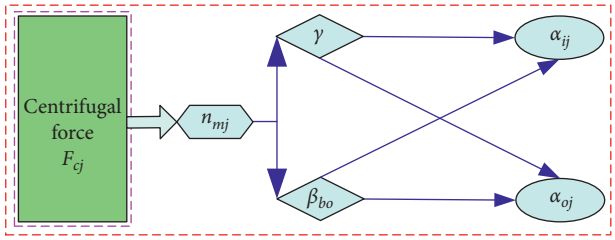

FIGURE 4: Analysis of the variable transfer relationship of centrifugal force F_{cj}.

where the calculation equations of the rotation speed $n_{bj}$of the rolling element can be expressed:

$$n_{bj} = \frac{d_m\left(1-\gamma_{ij}\right)\left(1+\gamma_{oj}\right)\left(\Omega_i \pm \Omega_o\right)}{D_w\left(1-\gamma_{ij}\right)\cos\left(\alpha_{oj}-\beta\right)+D_w\left(1+\gamma_{oj}\right)\cos\left(\alpha_i-\beta\right)}. \tag{24}$$

As shown in Figure 5, by substituting (20), (21), and (24) into (23), the variables recursive relation of gyroscopic moment M_{gj} can be obtained.

(3) Analysis of the Variables Recursive Relation of Contact Stiffnesses K_{ij} and K_{oj} at Contact Points. In ball angular position ψ_j, the contact stiffnesses K_{ij} and K_{oj} of high-speed angular ball bearing at contact points between the rolling elements and the inner and outer rings can be expressed as follows:

$$K_{ij} = 2.15\times10^5\left(\sum\rho_{ij}\right)^{-1/2}\left(n_\delta\right)^{-3/2}, \tag{25}$$

$$K_{oj} = 2.15\times10^5\left(\sum\rho_{oj}\right)^{-1/2}\left(n_\delta\right)^{-3/2}, \tag{26}$$

where the function of principal curvature $\sum\rho$ can be expressed:

$$\sum\rho = \rho_{1\mathrm{I}}+\rho_{2\mathrm{I}}+\rho_{1\Pi}+\rho_{2\Pi}. \tag{27}$$

For angular ball bearing: $\rho_{1\mathrm{I}} = \rho_{1\Pi} = 2/D_w$, $\rho_{2\mathrm{I}} = -1/f_jD_w$, and $\rho_{2\Pi} = \mp2\gamma/D_w(1\pm\gamma)$.

Then, the equation can be obtained:

$$\sum\rho_j = \frac{4}{D_w}+\frac{2\gamma_{jq}}{D_w\left(1\mp\gamma_{jq}\right)}-\frac{1}{f_iD_w}, \tag{28}$$

where minus was taken when $j = i$.

n_δ can be obtained by looking up the table based on the principal curvature difference function $F(\rho)$:

$$F(\rho) = \frac{\left(\rho_{12}-\rho_{11}\right)+\left(\rho_{22}-\rho_{21}\right)}{\sum\rho}. \tag{29}$$

Based on the above analysis, the variable transfer relationship of contact stiffnesses K_{ij} and K_{oj} are shown in Figure 6.

(4) Analysis of the Variables Recursive Relation of Contact Forces Q_{ij} and Q_{oj}. In ball angular position ψ_j, the contact forces Q_{ij} and $Q_{oj}$of high-speed angular ball bearing at

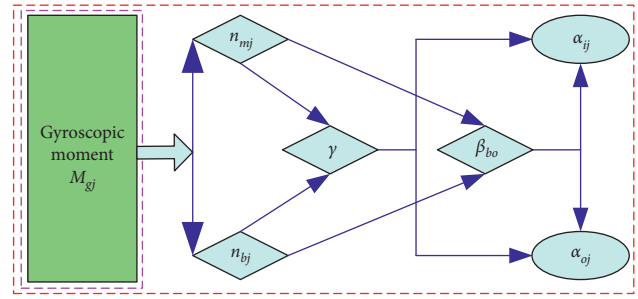

FIGURE 5: Analysis of variable transfer relationship of gyro moment M_{gj}.

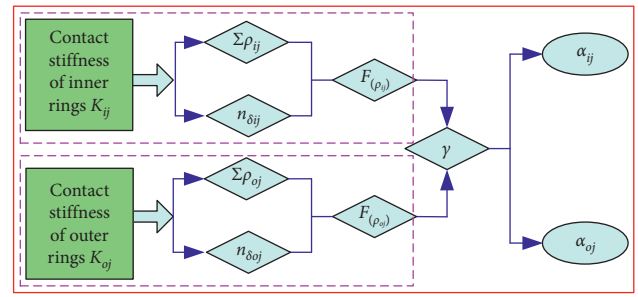

FIGURE 6: Analysis of variable transfer relationship of contact point stiffnesses K_{ij} and K_{oj}.

contact points between the rolling elements and the inner and outer rings can be expressed as follows:

$$Q_{ij} = K_{ij}\delta_{ij}^{1.5}, \tag{30}$$

$$Q_{oj} = K_{oj}\delta_{oj}^{1.5}. \tag{31}$$

Through the relations among (25)–(31), the transfer relations of contact force and variables can be obtained, as shown in Figure 7.

(5) Overall Analysis of Variable Recursion Relations. Based on the analysis of the above variables, such as centrifugal force F_{cj}, gyro moment M_{gj}, contact stiffnesses K_{ij} and K_{oj}, and contact forces Q_{ij} and Q_{oj}, the total transfer diagram of the variable transfer relationship of the dynamic characteristic equations can be obtained, as shown in Figure 8.

2.2.2. Derivation of Simplified Computational Models. Combining the relationship of variable transfer and dynamic characteristic equations, it is found that the eight basic variables X_{1j}, X_{2j}, δ_{ij}, δ_{oj}, K_{ij}, K_{oj}, F_{cj}, and M_{gj} are all functions of the actual internal and external contact angles α_{ij} and α_{oj}. It can be concluded that the actual internal and external contact angles α_{ij} and α_{oj} are the keys to solve and analyze the dynamic characteristic equations.

The system of nonlinear equations consists of (7), (8), (13), (14), and (16)–(18). It transforms $4Z$ basic unknown variables about X_{1j}, X_{2j}, δ_{ij}, and δ_{oj} in the equations into $2Z$ unknown variables about the actual internal α_{ij} and external contact angles α_{oj}. Then, it makes $4Z+2$ unknown variables X_{1j}, X_{2j}, δ_{ij}, δ_{oj}, δ_a, and δ_r of the original nonlinear

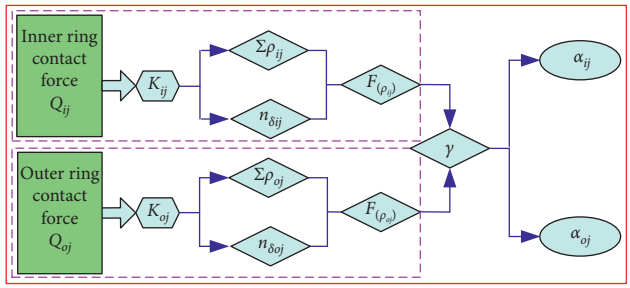

Figure 7: Analysis of variable transfer relationship of contact forces Q_{ij} and Q_{oj}.

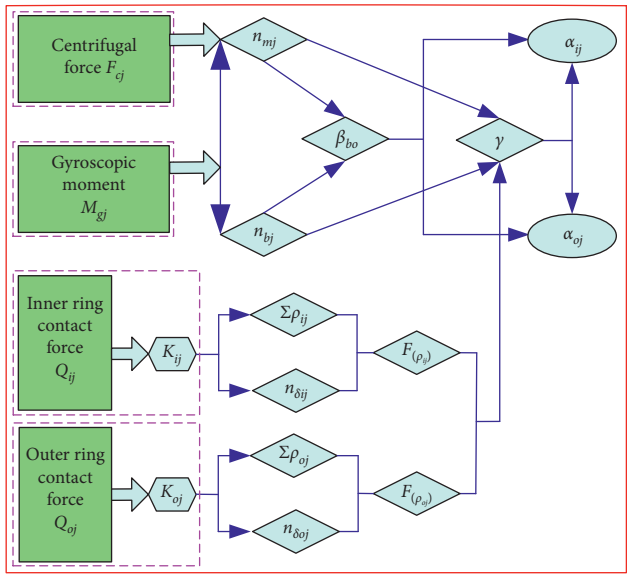

Figure 8: Dynamic characteristic equations variable transfer relationship total analysis diagram.

equations reduced to $2Z+2$ unknown variables α_{ij}, α_{oj}, δ_a, and δ_r. This reduces the dimension of the complex dynamic characteristic equations, makes the coupling hierarchy of the variables clear, reduces the iterative solution of the intermediate variables, and improves the convergence of the equations.

3. Solution of Computational Model Based on Improved Artificial Bee Colony Algorithm

3.1. Artificial Bee Colony Algorithm and Its Algorithm Structure Improvement. When the standard artificial bee colony algorithm solves the high-dimensional optimization problem, there is a disadvantage that the convergence speed becomes slower as the dimension increases and it is easy to fall into the local optimum and premature convergence when solving the problem of large root difference. Therefore, the standard artificial bee colony algorithm needs to be improved.

3.1.1. Improvements in Search Strategy. The standard artificial bee colony algorithm uses the same search formula for leading the bee phase and following the bee phase:

$$x'_{m,i} = x_{m,i} + \text{rand}(-1,1) * \left(x_{m,i} - x_{k,i}\right), \tag{32}$$

where $x_{k,i}$ is randomly selected from the existing food source x_m and $k \neq m$, rand $(-1, 1)$ represents a random number generated in the interval $(-1, 1)$.

The standard artificial bee colony algorithm uses the same search formula (32) in the leading bee stage and the following bee stage. Searching for the current food source x_m, the neighborhood of the current solution x_m, and in each cycle the global optimal solution is simply stored, but not in the search strategy, which plays the guiding role of the current global optimal solution to the real solution x_{best}. In order to improve the quality of the solution of the high-dimensional nonlinear problem and the global solution and convergence speed of the bee colony algorithm, the search formula (32) for the bee stage and follow-bee stages in the standard bee colony algorithm is improved to the following formula:

$$x'_{m,i} = x_{\text{best},i} + \text{rand}(-1,1) * \left(x_{\text{best},i} - x_{m,i}\right), \tag{33}$$

$$x'_{m,i} = x_{k,i} + \text{rand}(-1,1) * \left(x_{m,i} - x_{k,i}\right). \tag{34}$$

After improving the standard artificial bee colony algorithm, the leader bee uses the search formula (33) to search. It is based on the global optimal solution $x_{\text{best},i}$ and plays its guiding role. Meanwhile, combining with the current solution $x_{m,i}$, the leader bee carries out neighborhood search to obtain a better new solution $x'_{m,i}$. Similarly, the follower bee uses search formula (34) to search. It is based on the random selection of other food source solutions $x_{k,i}$ and uses the current solution $x_{m,i}$ to search the neighborhood to obtain a better new solution $x'_{m,i}$. Random selection of other food sources can enhance the global search ability of the algorithm and avoid single local search.

3.1.2. Algorithm Structure Improvement. The geometric parameters of high-speed angular contact ball bearings belong to centimeter level and the loaded deformation parameters belong to micrometer level, so the results of calculation model have great root differences. However, the standard artificial bee colony algorithm does not consider individual diversity and difference, so it is necessary to make structural improvements to the standard artificial bee colony algorithm.

Standard artificial bee colony algorithm generates N food sources directly in the initialization stage, that is, generating N D-dimensional initial solutions $x_m = (x_{m1}, x_{m2}, x_{mi}, \ldots, x_{mD})$, among them $m = 1, 2, 3, \ldots, D$, $i = 1, 2, 3, \ldots, D$. In the initialization stage, the cross-scale problem and priority relationship in each possible solution $x_{m1}, x_{m2}, x_{mi}, \ldots, x_{mD}$ are not considered step by step for the problem with large root differences. As a result, the algorithm converges to unreliable solutions prematurely and even falls into local dead cycles, which seriously affects the global convergence rate.

The author uses the idea of segmentation to initialize the parameters of the food source x_m: first generate parameters

δ_a and δ_r and then generate parameters α_{ij} and α_{oj}, which solves all the differences and cross-scale problems of the required parameters, so that the algorithm is reliable at the source and ensures the accuracy of the calculation results.

Some codes after adjusting the structure of the algorithm are shown in Table 1, which represents the parameters δ_a and δ_r; Table 2 represents the parameters α_{ij} and α_{oj} to be determined.

3.2. Testing and Analysis of Improved Algorithms. In order to verify the reliability and feasibility of the improved algorithm, four standard test functions are used to test the performance of the improved artificial bee colony algorithm. Among the four standard test functions, f_1 is the Rastrigin function, f_2 is the Ackley function, f_3 is the Rosenbrock function, and f_4 is the selfdef function, and its analytical expression is from (35) to (38).

Rastrigin function f_1 is

$$f_1(x) = 10n + \sum_{i=1}^{n} \left[x_i^2 - 10\cos(2\pi x_i)\right]. \tag{35}$$

Ackley function f_2 is

$$f_2(x) = -20\exp\left(0.2\sqrt{\frac{1}{n}\sum_{i=1}^{n} x_i^2} - \exp\left(\frac{1}{n}\sum_{i=1}^{n}\cos(2\pi x_i)\right)\right) + e + 20. \tag{36}$$

Rosenbrock function f_3 is

$$f_3(x) = \sum_{i=1}^{n}\left(100\left(x_i^2 - x_{i+1}\right)^2 + (x_i - 1)^2\right). \tag{37}$$

Selfdef function f_4 is

$$f_4(x, y) = \sqrt{\left((x - 9999)^2 + y^2 - 5\right)^2 + \left((x - 9998)y - \left(\frac{3x}{1000} + 1\right)\right)^2}. \tag{38}$$

In Figure 9, (a) is a three-dimensional diagram of a Rastrigin test function, (b) is a three-dimensional diagram of an Ackley test function, (c) is a three-dimensional diagram of a Rosenbrock test function, and (d) is a three-dimensional diagram of a Selfdef test function. f_1 is a multimodal function. In the domain $x_i \in [-5.12, 5.12]$, this function has very many minima, and there is only one minimum, and the global minimum is $\min(f_1) = f_1(0, 0, \ldots, 0) = 0$. The f_2 test function is used to verify the global convergence speed of the algorithm. The global minimum in the domain $x_i \in [-5, 5]$ is $\min(f_2) = f_2(0, 0, \ldots, 0) = 0$. f_3 is a complex morbid function. Because it is difficult to find its global minimum, it is necessary to use this function to test the improved artificial bee colony algorithm. In the domain of $x_i \in [-10, 10]$, the global minimum is $\min(f_3) = f_3(0, 0, \ldots, 0) = 0$. f_4 is used to test a function with a large root difference. This function is in the domain interval $x \in [-15000, 15000]$, and the minimum value is $\min(f_4) = f_4(10000, 2) = 0$. From Figure 9, it can intuitively observe the extreme value of each function.

Table 3 shows the maximum number of iterations, test dimensions, algorithm control parameters, theoretical global optimal solutions, and search range for the four test functions where f_1, f_2, and f_3 are used to test whether the algorithm has reliable global convergence speed and high accuracy in the face of high-dimensional, nonlinear, and multiextreme problems; f_4 is used to test whether the improved algorithm has reliable search ability for large root difference problems.

The test results show that the standard artificial bee colony algorithm and the improved artificial bee colony algorithm are used to calculate the results of 10 tests for each test function, as shown in Table 4. Meanwhile, the comparison curves of convergence rate of each test function are obtained, as shown in Figure 10.

From Table 4 and Figure 10, it can be seen that the improved algorithm improves in the order of magnitude compared with the standard algorithm in terms of the optimal solution accuracy, the worst solution accuracy, the mean value accuracy, and the variance accuracy. Meanwhile, the improved artificial bee colony algorithm reduces significantly the iteration calculation time compared with the standard artificial bee colony algorithm. These syntheses show that the improved artificial bee colony algorithm can solve the high-speed angular contact ball bearing calculation model with high dimension, nonlinearity, multiextremum, and large root difference.

3.3. Solution of Simplified Calculation Model. In order to adopt the improved artificial bee colony algorithm, the high-speed angular contact ball bearing calculation model needs to be simplified to the optimization calculation model. First, (7), (8), (13), (14), (16), and (17) are assembled into the following function groups:

Table 1: Initialization phase algorithm structure adjustment part of the code.

Generate δa, δr
(1) **def** calculate (self)
(2) rnd = np.random.random (size = self.len-2 ∗ self.z) # *example*: *if self.len* = 5, *rnd* = (*0.29049083 0.96149427 0.75*)
(3) **for** i, k **in** zip (range(0, self.len-2 ∗ self.z), range (0, self.len-2 ∗ self.z)):
(4) self.chrom 3(i) = self. bound (0, 2 ∗ self.z + i) + (self.bound (1, 2 ∗ self. z + i) − self.bound (0, 2 ∗ self. z + i)) ∗ rnd(k)
(5) **for** i **in** range (0, self.len-2 ∗ self.z):
(6) self.X (2 ∗ self.z + i) = self.chrom3(i) # δa, δr
#self.X (2 ∗ self.z + 1) = self.chrom3(2 ∗ self.z + 1)
#self.X (4 ∗ self.z + 2) = self.chrom(4 ∗ self.z + 2)
(7) super().some_necessary_calculations()
(8) r = 0
(9) **while r** < self.z:
(10) **if** self.A1 (r) < 0 or self.A2 (r) < 0:
(11) rnd = np.random.random (size = self.len-2 ∗ self.z) # *example*: *if self.len* = 5, *rnd* = (*0.29049083 0.96149427 0.75*)
(12) **for** i, k **in** zip (range (0, self.len-2 ∗ self.z), range (0, self.len - 2 ∗ self.z)):
(13) self.chrom3(i) = self.bound (0, 2 ∗ self.z + i) + (self.bound (1, 2 ∗ self.z + i) − self.bound (0, 2 ∗ self.z + i)) ∗ rnd (k) # xij=$x$min, j + rand (0, 1) ($x$max, j − $x$min, j)
(14) **for** i **in** range(0, self.len-2 ∗ self.z):
(15) self.X (2 ∗ self.z + i) = self.chrom3(i)
#self.X (2 ∗ self.z + 1) = self.chrom3(2 ∗ self.z + 1)
#self.X (4 ∗ self.z + 2) = self.chrom(4 ∗ self.z + 2)
(16) super().some_necessary_calculations()
(17) r = 0

Table 2: Initialization phase algorithm structure adjustment of another part of the code.

Generate α_i, α_o
#α_i
(1) rnd = np.random.random (size = self.z//2 + 1) # *example*: *if self.len* = 5, *rnd* = (*0.29049083 0.96149427 0.75*)
(2) rand1 = sorted (rnd) *#size* = 8
(3) **for** i **in** range (0,self.z//2 + 1):
(4) self.rand1(i) = rand1(i)
(5) **for** i **in** range(self.z//2 + 1,self.z):
(6) self.rand1(i) = self.rand1(self.z − i) *#size* = *16*
(7) **for** i, **k** in zip (range(0,self.z//2 + 1), range(0, self.z//2 + 1)):
(8) self.chrom1(i) = self.bound (0, i) + (self.bound (1, i) − self.bound (0, i)) ∗ self.rand1(k) # Xij = Xmin, j + *rand*
(9) **for** i **in** range (self.z//2 + 1,self.z):
(10) self.chrom1(i) = self.chrom1 (self.z − i)
#α_o
(11) rnd = np.random.random (size = self.z//2 + 1) # *example*: *if self.len* = 5, *rnd* = (*0.29049083 0.96149427 0.75*)
(12) rand2 = sorted (rnd,reverse = **True**) *#size* = *8*
(13) **for** i **in** range(0,self.z//2 + 1):
(14) self.rand2(i) = rand 2(i)
(15) **for** i **in** range (self.z//2 + 1,self.z):
(16) self.rand2(i) = self.rand2 (self.z − i) *#size* = *16*
(17) **for** i, **k in** zip (range (0, self.z//2 + 1), range (0, self.z//2 + 1)):
(18) self.chrom2(i) = self.boun ((0, i + self.z) + (self.bound (1, i + self.z) − self.bound (0, i + self.z)) ∗ self.rand2(k) # Xij = Xmin, j + rand (0, 1) (Xmax,j−Xmin, j) # *example*: *if self.len* = 5, *rnd* = (*0.29049083 0.96149427 0.75*)
(19) **for** i **in** range (self.z//2 + 1, self.z):
(20) self.chrom2(i) = self.chrom2 (self.z − i)

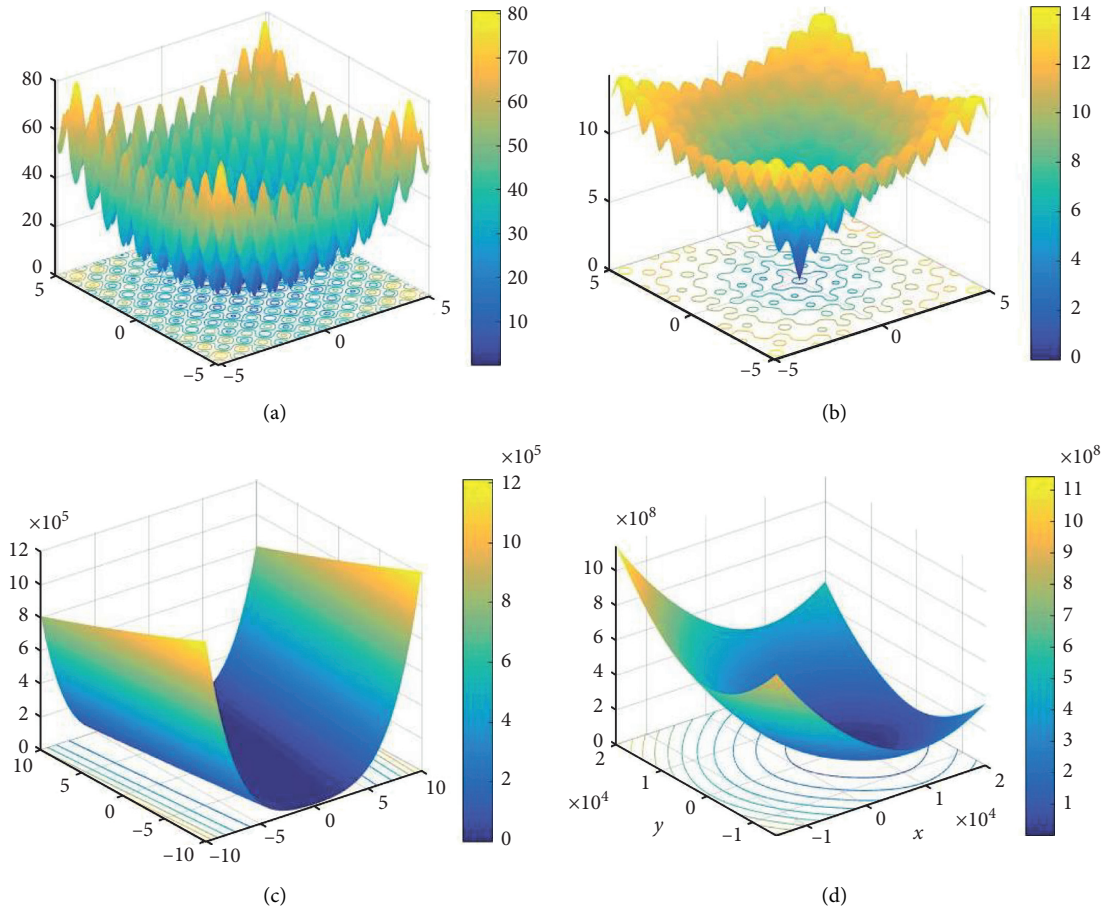

Figure 9: Three-dimensional visualization of standard test functions.

Table 3: Test functions and algorithm parameter settings.

Function	Maximum number of iterations	Functional dimension	Algorithmic control parameters	Population size	Theoretical global optimal solution	Search range
f_1	5000	50	100	30	0	[−5.12, 5.12]
f_2	5000	50	100	30	0	[−5, 5]
f_3	5000	50	100	30	0	[−10, 10]
f_4	5000	2	100	30	0	[−15000, 15000]

Table 4: Comparison of standard artificial bee colony algorithm and improved artificial bee colony algorithm.

Test function	Algorithm	Optimal solution	The worst solution	Mean	Standard deviation	Calculating time (s)
Rastrigin	Standard	$1.95284E-08$	$9.62104E-06$	$3.24631E-06$	$4.02246E-06$	27.94
	Improved	$3.64366E-10$	$2.30741E-09$	$4.78643E-10$	$7.56349E-10$	23.43
Ackley	Standard	$4.14784E-11$	$9.97926E-11$	$2.38264E-11$	$2.23417E-11$	33.65
	Improved	$6.43285E-13$	$7.15932E-12$	$8.13264E-13$	$2.78687E-12$	28.26
Rosenbrock	Standard	$1.41868E-02$	$5.23661E-01$	$4.23692E-01$	$1.97058E-01$	96.56
	Improved	$5.38452E-04$	$1.35267E-03$	$6.43285E-04$	$3.17665E-04$	73.24
Selfdef	Standard	$8.38282E-07$	$2.05764E-05$	$6.43657E-06$	$7.05824E-06$	23.68
	Improved	$1.57346E-08$	$8.43697E-08$	$3.85145E-08$	$2.46283E-08$	17.35

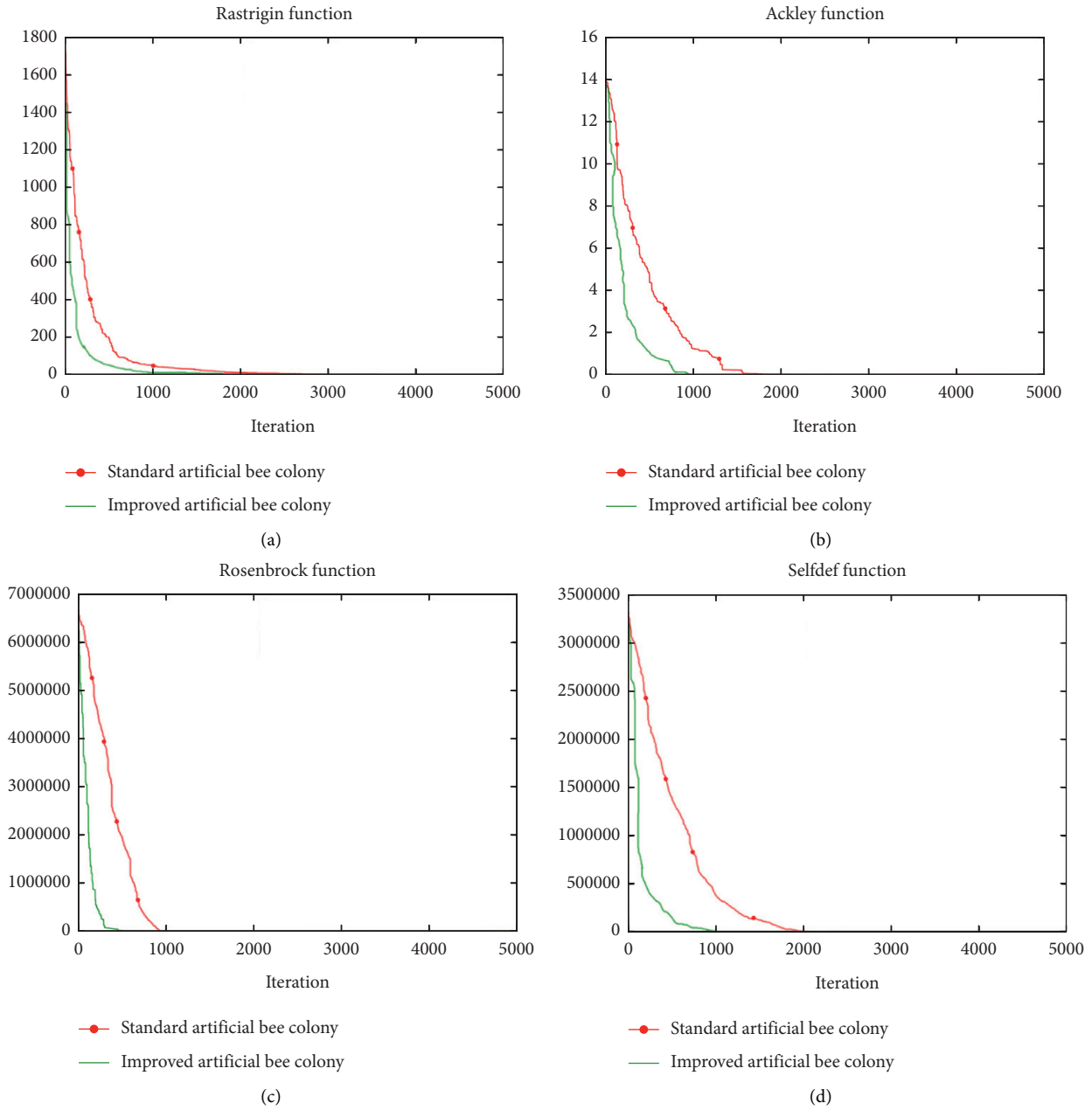

Figure 10: Convergence rate contrast curve. (a) Rastrigin function. (b) Ackley function. (c) Rosenbrock function. (d) Selfdef function.

$$\begin{cases} F_{1j} = \left(A_{1j} - X_{1j}\right)^2 + \left(A_{2j} - X_{2j}\right)^2 - \left[(f_i - 0.5)D + \delta_{ij}\right]^2, \\ F_{2j} = X_{1j}^2 + X_{2j}^2 - \left[(f_o - 0.5)D + \delta_{oj}\right]^2, \\ F_{3j} = \dfrac{K_{ij}\delta_{ij}^{1.5}\left(A_{1j} - X_{1j}\right) - \left(\lambda_{ij}M_{gj}/D\right)\left(A_{2j} - X_{2j}\right)}{(f_i - 0.5)D + \delta_{ij}} + \dfrac{\left(\lambda_{oj}M_{gj}X_{2j}/D\right) - K_{oj}\delta_{oj}^{1.5}X_{1j}}{(f_o - 0.5)D + \delta_{oj}}, \\ F_{4j} = \dfrac{K_{ij}\delta_{ij}^{1.5}\left(A_{2j} - X_{2j}\right) - \left(\lambda_{ij}M_{gj}/D\right)\left(A_{1j} - X_{1j}\right)}{(f_i - 0.5)D + \delta_{ij}} - \dfrac{\left(\lambda_{oj}M_{gj}X_{1j}/D\right) + K_{oj}\delta_{oj}^{1.5}X_{2j}}{(f_o - 0.5)D + \delta_{oj}} + F_{cj}, \\ F_{5j} = F_a - \sum_{j=1}^{j=z}\left[\dfrac{K_{ij}\delta_{ij}^{1.5}\left(A_{1j} - X_{1j}\right) - \left(\lambda_{ij}M_{gj}/D\right)\left(A_{2j} - X_{2j}\right)}{(f_i - 0.5)D + \delta_{ij}}\right]. \\ F_{6j} = F_r - \sum_{j=1}^{j=z}\left[\dfrac{K_{ij}\delta_{ij}^{1.5}\left(A_{2j} - X_{2j}\right) - \left(\lambda_{ij}M_{gj}/D\right)\left(A_{1j} - X_{1j}\right)}{(f_i - 0.5)D + \delta_{ij}}\right]\cos\psi_j. \end{cases} \tag{39}$$

Substituting (32)–(35) into function group (36), then transforming functions F_{1j}, F_{2j}, F_{3j}, F_{4j}, F_{5j}, and F_{6j} into objective functions, and finally using improved artificial bee colony algorithm to find Minimum value, the specific optimization model is as follows:

Objective function:

$$F = \sqrt{\sum_{j=1}^{Z} F_{1j}^2 + \sum_{j=1}^{Z} F_{2j}^2 + \sum_{j=1}^{Z} F_{3j}^2 + \sum_{j=1}^{Z} F_{4j}^2 + F_5^2 + F_6^2}. \tag{40}$$

The design variables are

$$x = \left(\alpha_{i1}, \alpha_{i2}, \alpha_{i3}, \ldots, \alpha_{ij}, \alpha_{o1}, \alpha_{o2}, \alpha_{o3}, \ldots, \alpha_{oj}, \delta_a, \delta_r\right). \tag{41}$$

The basic constraints are

$$\begin{aligned} 0 \le \alpha_{ij} \le \alpha^0, \\ \alpha^0 \le \alpha_{ij} \le \alpha rc\sin\left(\frac{A_{1j} - X_{1j}}{(f_i - 0.5)D + \delta_{ij}}\right). \end{aligned} \tag{42}$$

Find $x$to minimize the $F(x)$ value; that is, find $\min F(x)$.

The design variables are $2Z + 2$, which are nearly half less than the solution variables of the traditional numerical algorithm and are conducive for improving the global convergence rate. The specific flow of the high-speed angular contact ball bearing calculation model using the improved artificial bee colony algorithm is shown in Figure 11.

4. Results and Discussion

Taking 218 high-speed angular contact ball bearings as an example, the author analyzes and calculates its dynamic characteristics. The specific geometric structure parameters and material parameters are shown in Table 5, and the working condition parameters are given according to the specific analysis.

4.1. Calculation Results Accuracy Verification. In order to verify the accuracy of the deformation calculation, the bearing stiffness test bench, as shown in Figure 12, was used to measure the axial deformation of the high-speed angular contact bearing, under the action of both axial and radial forces.

Figure 13 shows the axial deformation of the inner ferrule under different axial forces. Figure 14 shows the axial deformation of the inner ferrule when the bearing is subjected to both axial and radial forces. Meanwhile, Figures 13 and 14, respectively, compare the experimental results with the numerical results of the improved algorithm. It can be shown from Figure 13 that the axial deformation increases with the increase of axial force and velocity, respectively. When the axial load is low and the rotation speed is high, the axial deformation will be negative due to the centrifugal force of the rolling element. With the axial force increases, the axial deformation gradually changes from negative to positive. It can be seen from Figure 14 that the axial deformation also increases with the increase of the axial force and speed, respectively. This condition is consistent with the axial change trend of pure axial load, and it shows that the radial force has little effect on the axial deformation.

It can be seen from Figures 13 and 14 that the numerical calculation results are basically consistent with the trend of the test results; there is a certain deviation between the two sets of data, which is due to the assumption of ring deformation in the numerical algorithm and the absence of consideration of bearing clearance and other factors. Furthermore, the results data of the change trend of the above

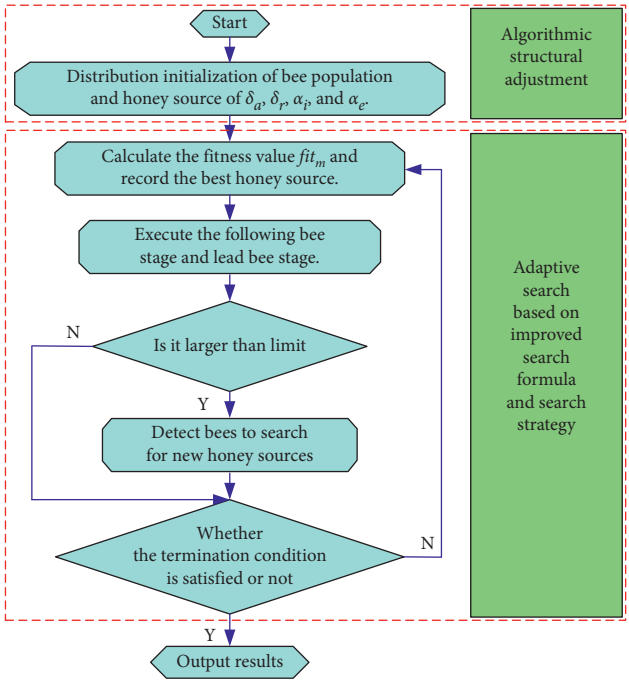

Figure 11: Solution flow chart.

Table 5: Structural parameters and material parameters of 218 angular contact ball bearings.

Bearing structural and material parameters	Numerical value
Inner raceway diameter (mm)	102.79
Outer raceway diameter (mm)	147.73
Rolling elements diameter (mm)	22.23
Number of rolling elements Z	16
The inner raceway curvature radius coefficient f_i	0.5232
The outer raceway curvature radius coefficient f_o	0.5232
Initial contact angel α^0 (o)	40
Rolling elements and inner and outer ring elastic modulus (GPa)	206
Rolling elements and inner and outer ring Poisson's ratio μ	0.3
Rolling elements and inner and outer ring density ρ (kg/m^3)	7850

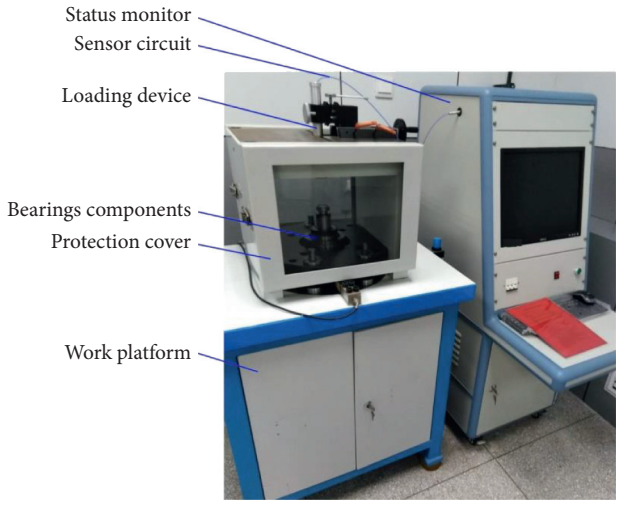

Figure 12: Bearing dynamic stiffness tester.

axial deformation is completely consistent with the calculation results in the literature [17, 24, 25].

4.2. Analysis of High-Speed Characteristic Calculation Results of Angular Contact Ball Bearing. The improved artificial bee colony algorithm was used to calculate the contact force between the ball and the inner and outer channels under different speeds and axial preloads. The calculation results are shown in Figures 15 and 16, respectively.

It can be seen from Figure 15 that the internal contact force increases linearly with the increase of axial force; at the same speed, the internal contact force increases substantially with the increase of axial force. Under the same axial force, the internal contact force decreases with the increase of rotating speed, and the decreasing range is smaller and smaller.

It can be seen from Figure 16 that when the rotation speed is low, the external contact force increases linearly with the increase of the axial force; thus the increase

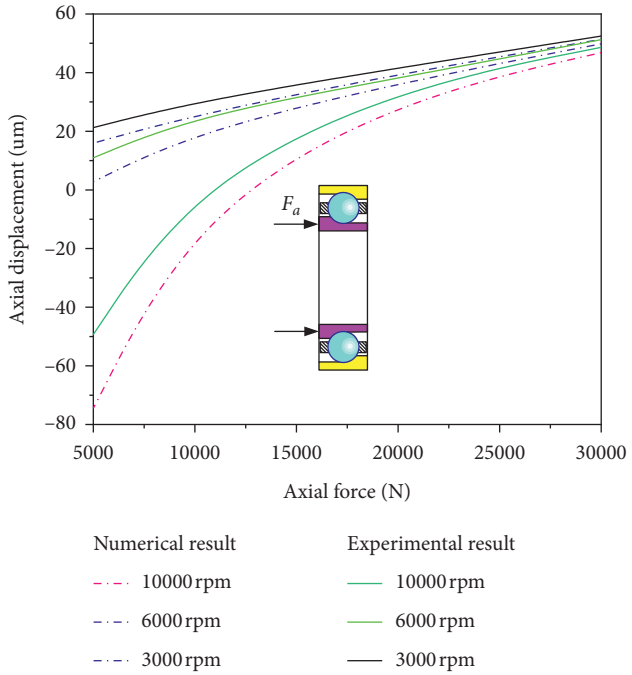

Figure 13: Axial deformation only under axial load.

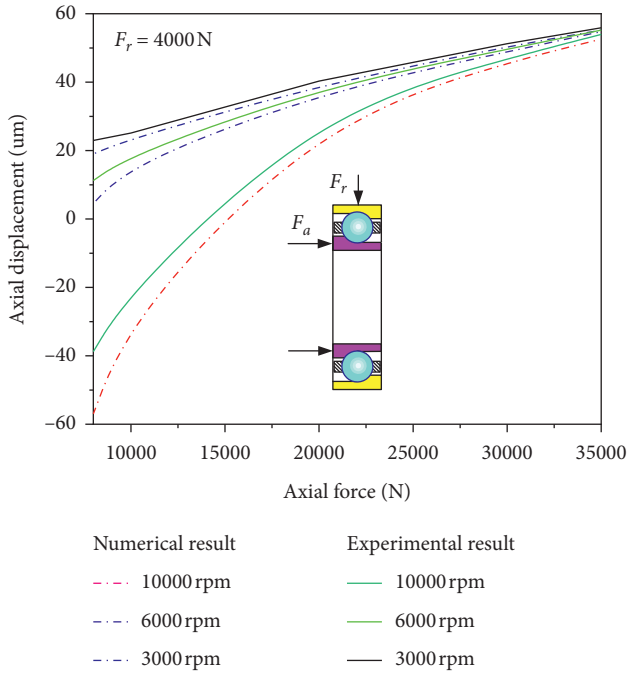

Figure 14: Axial deformation under axial load and radial load.

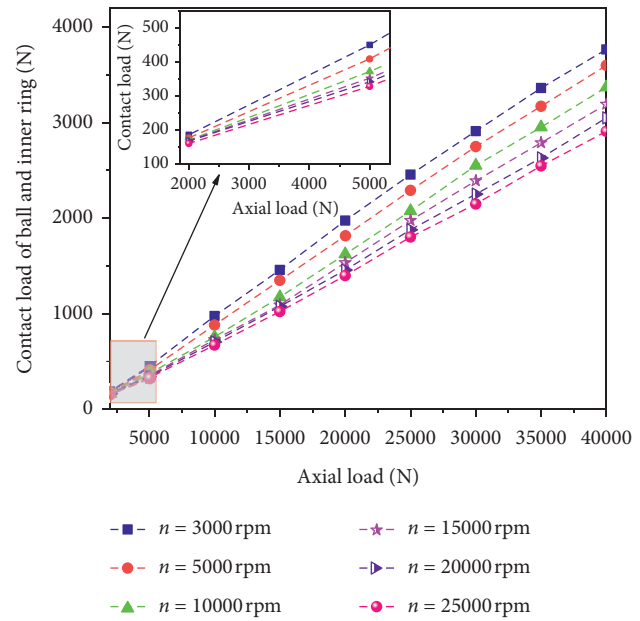

Figure 15: The contact force between inner ring and rolling ball.

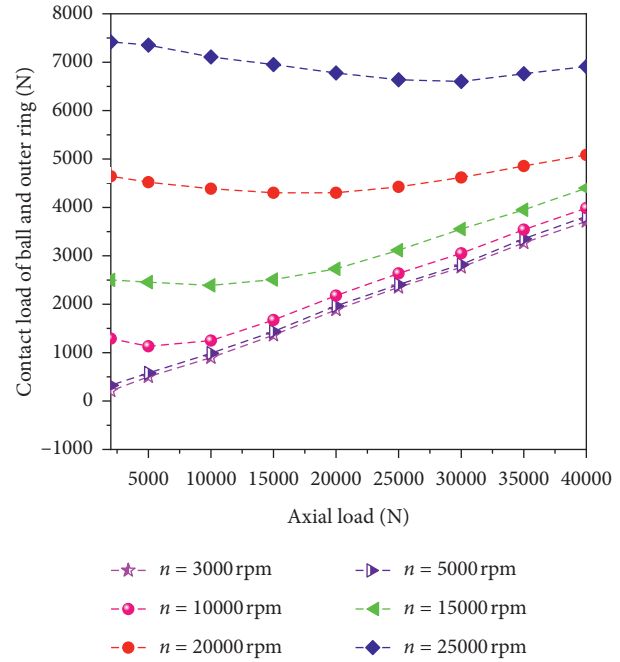

Figure 16: The contact force between outer ring and rolling ball.

amplitude is small. That is because, at low speed, the centrifugal force is also small, and the external contact force is mainly provided by axial force. When the rotation speed is high, the external contact force decreases first and then increases with the increase of axial force. That is because, at high speed, the centrifugal force is large, and when the axial force is small, the external contact force is mainly provided by the centrifugal force. With the axial force increases, the revolution speed of the rolling element and the inner and outer rings and the rolling element changes, resulting in the decrease of the centrifugal force and the decrease of the external contact force. As the axial force continues to increase, the external contact force is mainly provided by the axial force, which in turn causes the external contact force to increase as the axial force increases.

Figure 17 shows the change of the actual contact angle with the ball angle position under the same axial load and the change of the radial force load. It can be seen that when the

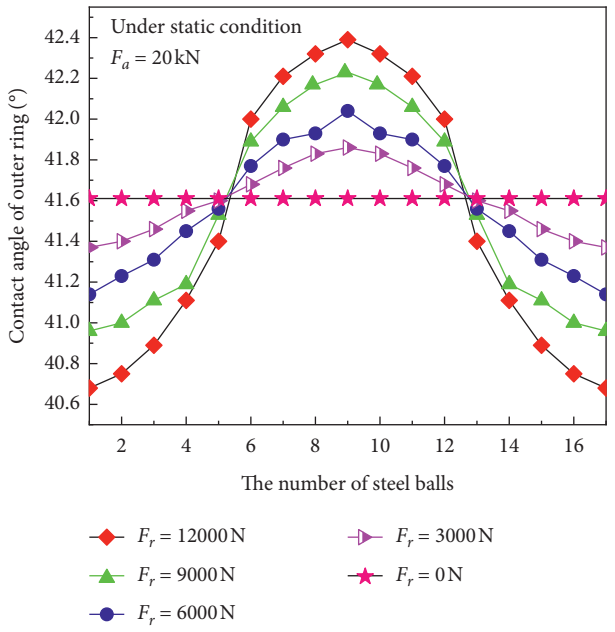

Figure 17: Change curve of actual contact angle with ball position under different radial loads.

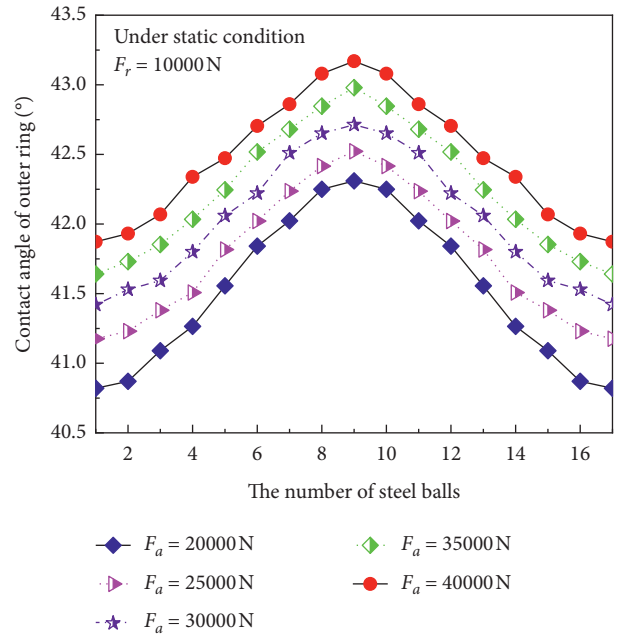

Figure 18: Change curve of actual contact angle with ball position under different axial loads.

influence of rotational speed is not considered and the radial force is zero, the actual contact angle is greater than the initial contact angle and does not change with the change of the ball position. When the radial force is greater than zero, the contact angle changes with the change of the ball position, and the minimum contact angle appears at the top of the ball in the opposite direction of the maximum radial force. That is because the contact force is minimal when the ball is in this position. The maximum position of contact angle is located at the top of the maximum radial force positive direction; meanwhile, the contact load acting on the ball is the largest. In addition, when the axial force is fixed, with the increase of the radial force, the change range of the actual contact angle of the bearing increases.

Figure 18 shows the change of the actual contact angle with the ball angle position under the same radial load and the change of the axial force load. It can be seen that the axial force only affects the actual contact angle of the ball bearing and does not change the distribution of the actual contact angle. And the actual contact angle of a ball bearing increases with increasing axial force.

Figure 19 shows the influence of rotation speed on the contact force between the ball and the inner ring when the bearing subjects both axial and radial forces. It can be seen from the figure that, within the range of the ball angles I and IV zones, the internal contact force increases with the increase of the rotation speed and the increase of the IV zone becomes gentle with the increase of the rotation speed. In zone II of ball angle, the internal contact force decreases with the increase of rotation speed. In the range of zone III of ball angle, it is a mixed change zone. With the increase of rotation speed, the change of the internal contact force has no obvious regularity.

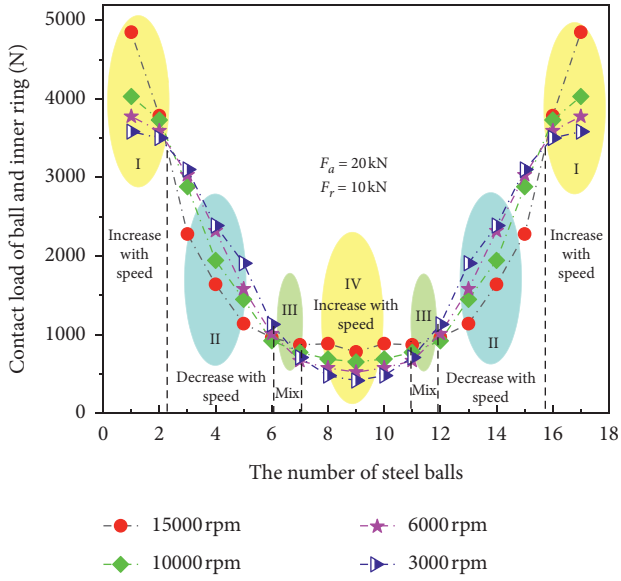

Figure 19: Contact force between ball and inner ring under axial force and radial force.

Figure 20 shows the influence of rotation speed on contact force between ball and outer ring under the condition of bearing both axial force and radial force. It can be seen from the figure that, in the range of zone I and zone III of ball angle, the external contact force increases with the increase of rotating speed. With the increase of rotating speed, the range of change in zone III becomes smaller and smaller due to the influence of centrifugal force and gyroscopic moment. In the range of zone II of ball angle, it is a mixed change zone. With the increase of rotation speed, the

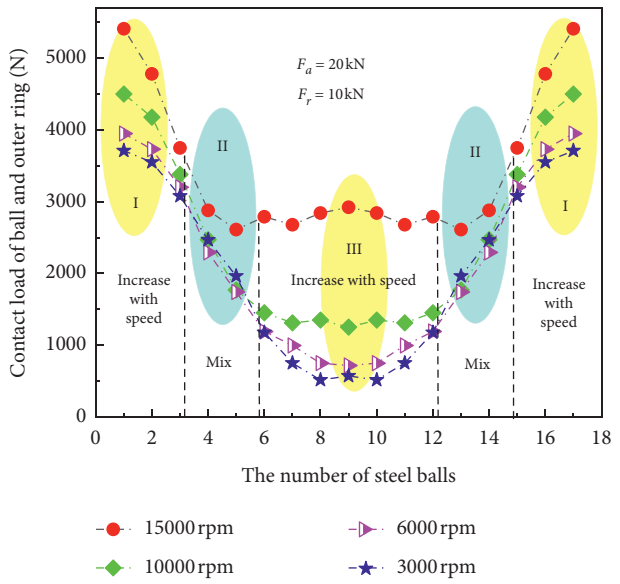

Figure 20: Contact force between ball and outer ring under axial force and radial force.

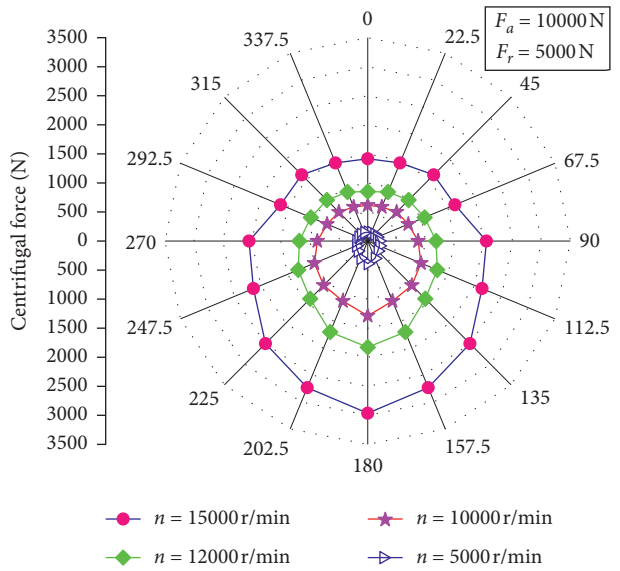

Figure 21: The variation of centrifugal force with different positions of rolling elements at different rotational speeds.

change of the internal contact force has no obvious regularity.

Figure 21 shows the influence of rotating speed on centrifugal force under the condition of bearing both axial force and radial force. As can be seen from the figure, the centrifugal force is particularly small at low speeds, and there is little difference in centrifugal force at different azimuths. As the speed increases, the centrifugal force increases sharply, and the gap between centrifugal forces at different azimuth angles also increases significantly.

Figure 22 shows the effect of the rotational speed on the gyro torque under the condition that the bearing is subjected to both axial and radial forces. It can be seen from the figure

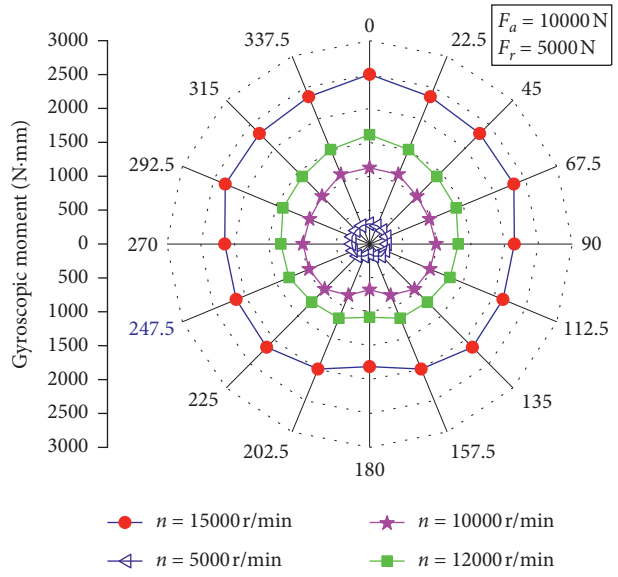

Figure 22: The variation of gyroscopic moment with different positions of rolling elements at different speeds.

that, under the same working conditions, the gyro torque of the rolling body increases with the increase of the rotation speed. When the speed $n > 5000r$/min, the gyro torque increases sharply. The gyro torque will cause the gyro to rotate, and the gyro will cause friction and heat, which will affect the performance of the bearing. Moreover, the variation range of the gyro torque of the rolling element increases with the increase of the rotating speed, and the gyro torque in the bearing area is larger than that in the nonload bearing area.

Meanwhile, the change trend results data of the above the actual contact angle, contact force, centrifugal force, and gyroscopic moment were completely consistent with the calculation result in the literatures [14, 24–27]. This verifies the correctness of the simplified model and the improved numerical algorithm to some extent.

5. Conclusion

According to the dynamic changes of various parameters of the angular contact ball bearing during high-speed operation, the equations for solving the high-speed dynamic characteristics are systematically analyzed.

(1) The transfer relationship of variables in the high-speed angular contact bearing model is explored, and a set of nonlinear equations with actual internal (inner) contact angle, actual external (outer) contact angle, radial deformation, and axial deformation as basic iterative variables are obtained. The number of nonlinear equations to be solved is greatly reduced.

(2) An artificial bee colony algorithm is proposed to solve the big root difference through algorithm improvement. The effectiveness of the improved algorithm is verified by the standard test function. The improved algorithm is applied to solve the

dynamic characteristics of high-speed angular contact ball bearings and is verified by a practical project.

(3) The model is used to solve the influence of the rotational speed on the actual contact angle, contact force, centrifugal force, gyroscopic moment, and attitude angle, which provides a reference for the use, research, and design of the high-speed angular contact bearing.

Data Availability

The data used to support the findings of this study are included within the article.

Conflicts of Interest

The authors declare that they have no conflicts of interest.

Acknowledgments

The authors would like to thank the National Key Research and Development Project of China (no.2018YFB1308701), Key Scientific and Technological Projects in Henan Province (162300410060), Shanxi Coal Based Low Carbon Joint Fund (no.U1610118), National Natural Science Foundation of China (no. 51375325), the Shanxi Provincial Special Fund for Coordinative Innovation Center of Taiyuan Heavy Machinery Equipment, and the fund for Shanxi "1331 Project" Key Subjects Construction for their support in this research.

References

[1] G. Zeng, C. Zhao, X. Yu et al., "Analysis of high speed bearing based on virtual rods model," *Journal of Mechanical Science and Technlogy*, vol. 34, no. 5, pp. 2133–2143, 2019.

[2] A. B. Jones, "Ball motion and sliding friction in ball bearings," *Journal of Basic Engineering*, vol. 81, no. 1, pp. 1–12, 1959.

[3] T. A. Harris and M. H. Mindel, "Rolling element bearing dynamics," *Wear*, vol. 23, no. 3, pp. 311–337, 1973.

[4] Y.-H. Yu, B.-R. Lee, and Y.-J. Cho, "New load distribution method for one-row slewing ball bearing considering retainer force," *International Journal of Precision Engineering and Manufacturing*, vol. 18, no. 1, pp. 49–56, 2017.

[5] K. Yan, B. Yan, Y. Wang, J. Hong, and J. Zhang, "Study on thermal induced preload of ball bearing with temperature compensation based on state observer approach," *International Journal of Advanced Manufacturing Technology*, vol. 94, no. 9-12, pp. 3029–3040, 2019.

[6] X. T. Bai, Y. H. Wu, I. C. Rosca, K. Zhang, and H. T. Shi, "Investigation on the effects of the ball diameter difference in the sound radiation of full ceramic bearings," *Journal of Sound and Vibration*, vol. 450, pp. 231–250, 2019.

[7] G. Liu, J. Hong, W. Wu, and Y. Sun, "Investigation on the influence of interference fit on the static and dynamic characteristics of spindle system," *International Journal of Advanced Manufacturing Technology*, vol. 99, no. 5-8, pp. 1953–1966, 2018.

[8] L. Oktaviana, V.-C. Tong, and S.-W. Hong, "Skidding analysis of angular contact ball bearing subjected to radial load and angular misalignment," *Journal of Mechanical Science and Technology*, vol. 33, no. 2, pp. 837–845, 2019.

[9] S.-W. Hong and V.-C. Tong, "Rolling-element bearing modeling: a review," *International Journal of Precision Engineering and Manufacturing*, vol. 17, no. 12, pp. 1729–1749, 2016.

[10] S. Deng, X. Li, and J. Wang, "Frictional torque characteristic of angular contact ball bearings," *Journal of Mechanical Engineering*, vol. 47, no. 5, pp. 114–120, 2011.

[11] T. Xu, L. Yang, and K. Wang, "Characteristics of duplex angular contact ball bearing with combined external loads and angular misalignment," *Applied Sciences*, vol. 10, no. 17, p. 5756, 2020.

[12] T. A. Harris, *Rolling Bearing analysis*, John Wiley & Sons, New York, NY, USA, 2001.

[13] J.-F. Antoine, G. Abba, and A. Molinari, "A new proposal for explicit angle calculation in angular contact ball bearing," *Journal of Mechanical Design*, vol. 128, no. 3, pp. 468–479, 2006.

[14] J. Zhang, B. Fang, K. Yan et al., "A novel model for high-speed angular contact ball bearing by considering variable contact angles," *Journal of Mechanical Science and Technology*, vol. 11, no. 3, 2020.

[15] E. Kurvinen, J. Sopanen, and A. Mikkola, "Ball bearing model performance on various sized rotors with and without centrifugal and gyroscopic forces," *Mechanism and Machine Theory*, vol. 90, pp. 240–260, 2015.

[16] B. Sun, X. Yu, Y. Hu et al., "Variable scale particle swarm optimization algorithm and application of nonlinear equations for high-speed ball bearings," *Bearing*, vol. 6, pp. 19–22, 2013.

[17] W.-Z. Wang, L. Hu, S.-G. Zhang, and L.-J. Kong, "Modeling high-speed angular contact ball bearing under the combined radial, axial and moment loads," *Proceedings of the Institution of Mechanical Engineers, Part C: Journal of Mechanical Engineering Science*, vol. 228, no. 5, pp. 852–864, 2014.

[18] B. Fang, J. Zhang, J. Hong, and Y. Zhu, "Quick calculation method and contact angle Analysis for high—speed angular contact ball bearing under combined loads," *Journal of Xi'an Jiao Tong University*, vol. 51, no. 6, pp. 115–121, 2017.

[19] C. G. Broyden, "Quasi-Newton methods and their application to function minimisation," *Mathematics of Computation*, vol. 21, no. 99, p. 368, 1967.

[20] A. Ben-Israel, "A Newton-Raphson method for the solution of systems of equations," *Journal of Mathematical Analysis and Applcations*, vol. 15, no. 2, pp. 243–252, 1996.

[21] G. S. S. V. Krishna Mohan and Y. S. Rao, "An efficient design of finite impulse response - fractional order differentiator using shuffled frog leaping algorithm heuristic," *International Journal of Wavelets, Multiresolution and Information Processing*, vol. 21, no. 3, 2019.

[22] A. Kaveh and M. R. Seddighian, "Simultaneously multi-material layout, and connectivity optimization of truss structures via an Enriched Firefly Algorithm," *Structures*, vol. 27, pp. 2217–2231, 2020.

[23] D. Karaboga and B. Basturk, "A powerful and efficient algorithm for numerical function optimization: artificial bee colony (ABC) algorithmficient algorithm for numerical function optimization: artificial bee colony (ABC) algorithm," *Journal of Global Optimization*, vol. 39, no. 3, pp. 459–471, 2007.

[24] L. Wang, L. Cui, D. Zheng et al., "Analysis on dynamic characteristics of aero-engine high-speed ball bearings," *Acta Aeronautica Et Astronautica Sinica*, vol. 18, 2007.

[25] Y. Tang, D. Gao, and G. Luo, "Research of aero-engine high-speed ball bearing," *Hangkong Dongli Xuebao/Journal of Aerospace Power*, vol. 21, no. 2, pp. 354–360, 2006.

[26] C. Zhao, X. Yu, Q. Huang et al., "Analysis on the load characteristics and coefficient of friction of angular contact ball bearing at high speed," *Tribology International*, vol. 87, no. 7, pp. 50–56, 2015.

[27] W.-Z. Wang, L. Hu, S.-G. Zhang, Z.-Q. Zhao, and S. Ai, "Modeling angular contact ball bearing without raceway control hypothesis," *Mechanism and Machine Theory*, vol. 82, pp. 154–172, 2014.